Tsinghua Science and Technology

Volume 23 | Issue 2 Article 1

2018

Effects of Power Inversion Spatial Only Adaptive Array on GNSS Receiver Measurements

Hailong Xu
the Department of Electronic Engineering, Tsinghua University, Beijing 100084, China.

Xiaowei Cui
the Department of Electronic Engineering, Tsinghua University, Beijing 100084, China.

Mingquan Lu
the Department of Electronic Engineering, Tsinghua University, Beijing 100084, China.

TSINGHUA SCIENCE AND TECHNOLOGY
ISSN 1007-0214 06/09 pp172–183
DOI: 10.26599 / TST.2018.9010019
Volume 23, Number 2, April 2018

Effects of Power Inversion Spatial Only Adaptive Array on GNSS Receiver Measurements

Hailong Xu, Xiaowei Cui*, and Mingquan Lu

Abstract: The Spatial Only Processing Power Inversion (SOP-PI) algorithm is frequently used in Global Navigation Satellite System (GNSS) adaptive array receivers for interference mitigation because of its simplicity of implementation. This study investigates the effects of SOP-PI on receiver measurements for high-precision applications. Mathematical deductions show that if an array with a centro-symmetrical geometry is used, ideally, SOP-PI is naturally bias-free; however, this no longer stands when non-ideal factors, including array perturbations and finite-sample effect, are added. Simulations are performed herein to investigate how exactly the array perturbations affect the carrier phase biases, while diagonal loading and forward-backward averaging are proposed to counter the finite-sample effect. In conclusion, whether SOP-PI with a centro-symmetrical array geometry will satisfy the high precision demands mainly depends on the array perturbation degree of the element amplitude and the phase center.

Key words: Global Navigation Satellite System (GNSS) receiver; adaptive array; high-precision application; power inversion; measurement bias; array perturbation; diagonal loading; forward-backward averaging

1 Introduction

Due to the limited power of Global Navigation Satellite System (GNSS) signals reaching the earth surface, interference, both intentional and unintentional, is one of the most jeoparding sources of performance degradation, and even denial-of-service, of GNSS receivers. Of all the alternatives to counter this issue, those based on the adaptive antenna array architecture are the most promising and widely used, especially for high-grade receivers with high demands of reliability and robustness[1–4].

The simplest candidate of all the adaptive array algorithms is the Spatial Only Processing Power Inversion (SOP-PI) algorithm. SOP-PI has a working mechanism that utilizes spatial Degrees Of Freedom (DOF) provided by multiple antennas to perceive the characteristics of the interference environment and adjust the antenna beam pattern to form nulls toward the interferences[5, 6]. This algorithm is easier to implement compared to the other alternatives not only because it does not need to know the incident directions of either the desired satellite signals or the interferences as prerequisites such that the Inertial Measurement Unit (IMU) equipped to measure the attitude of the antenna array plane is saved, but also because the SOP is less costly in the computational aspect compared to the Spatial Temporal Adaptive Processing (STAP) and the Spatial Frequency Adaptive Processing (SFAP)[5, 7, 8]. The only drawback of SOP-PI is that it cannot guarantee the beam pattern gains toward the satellites; hence, the received desired signals may risk suffering from Signal-to-Noise Ratio (SNR) attenuation and loss of tracking when their incident directions are in or close to the nulls. However, with the increasing number of satellites being deployed in multiple GNSS constellations, many visible satellites that are out of the nulls to be tracked by the

• Hailong Xu, Xiaowei Cui, and Mingquan Lu are with the Department of Electronic Engineering, Tsinghua University, Beijing 100084, China. E-mail: xuhl07@163.com; cxw2005@mail.tsinghua.edu.cn; lumq@mail.tsinghua.edu.cn.

* To whom correspondence should be addressed.
Manuscript received: 2017-01-17; accepted: 2017-04-09

receiver are scattered in the sky most of the time. In short, the ease of implementation and the limited degradation to the navigation and positioning performance make SOP-PI typical for use in receivers with ordinary accuracy requirements.

Traditionally, multi-antenna receivers are not proper for use in high-precision applications because of the measurement biases induced by the antenna array[3, 4, 7]. However, with the application fields of the GNSS expanding and the electromagnetic environment, where receivers reside, becoming more complicated, some kinds of high-precision receivers based on carrier phase measurements also put forward the demand for interference protection, such as in the scenes of sea-based aircraft landing[9] and vehicle attitude determination using Real Time Kinematic (RTK) in battlefields. To meet this demand, adaptive arrays should be adopted, and the measurement biases should be eliminated using some methods. Literatures have proposed multiple solutions in recent years. Some of them introduced bias-free constraints to the algorithms[10–12], while others compensated for those biases with estimated values at the tracking channel outputs[13–15]. Unfortunately, these methods cannot be used by PI because they all presumed the incident directions of the satellite signals. Thus, an elaborated study on how SOP-PI can meet high precision requirements is needed.

This study investigates how SOP-PI affects the measurement accuracy in GNSS receivers. The prerequisites with which SOP-PI can meet the high precision requirements are also provided. First, theoretical derivation is used to show that SOP-PI is naturally bias-free in the ideal case with a centro-symmetrical array geometry. However, measurement biases still occur because of non-ideal factors, such as array perturbations of the element amplitude, phase, and phase center caused by real antenna manufacturing, as well as the finite-sample effect in the algorithm implementation. The simulations for the array perturbations are performed to reveal how severe the carrier phase biases are while the perturbation degree varies. In addition, two countermeasures (i.e., diagonal loading and forward-backward averaging) are proposed for the finite-sample effect. The simulation results show that the SOP-PI implemented on a centro-symmetrical array can meet the high precision requirements as long as the array perturbations are small enough. Our study begins with modeling the antenna array and the signals, as well as the SOP-PI algorithm.

2 Signal Model and Algorithm

This section first presents the models of the signals and the antenna array, then provides a brief review of the SOP-PI algorithm.

Figure 1 shows the local antenna coordinate system, in which the array panel is located in the $X-Y$ plane, and the Z axis points to the upper hemisphere along the normal direction of the array. The incident direction of the desired satellite signal or the interference is depicted by the angle pair (θ,ϕ), with θ as the angle off the Z axis and ϕ as the angle off the X axis within the $X-Y$ plane. Thus, the incident vector is presented as follows:

$$\boldsymbol{a}=-\left[\sin\theta\cos\phi,\ \sin\theta\sin\phi,\ \cos\theta\right]^{\mathrm{T}} \tag{1}$$

This study exploited a seven-element array as a demonstration. Figure 2 presents its geometry on the left. The array was made up of six equally spaced elements on a circle with the radius half the wavelength of the carrier frequency and a reference element at the circle center, which was also the coordinate origin. The position of the n-th element is denoted by vector $\boldsymbol{p}_n$. This kind of geometry was called herein as the "centro-symmetry", meaning that except for the reference element at the coordinate origin, there must be an identical element at $-\boldsymbol{p}_n$ for every element located at $\boldsymbol{p}_n$. Multiple array geometries satisfied this condition, and the analysis and conclusions of this paper applied to all of them. Another centro-symmetrical array with five elements was presented in Fig. 2 on the right.

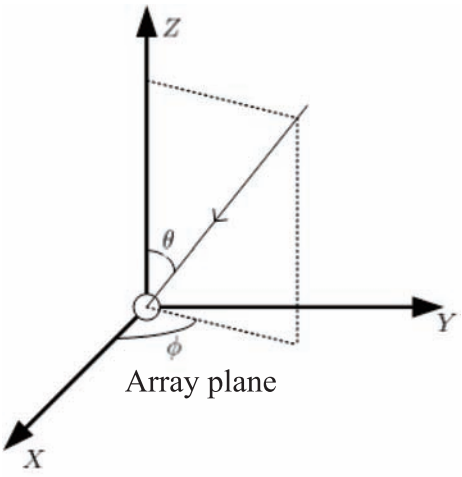

Fig. 1 Local antenna coordinate system and incident direction.

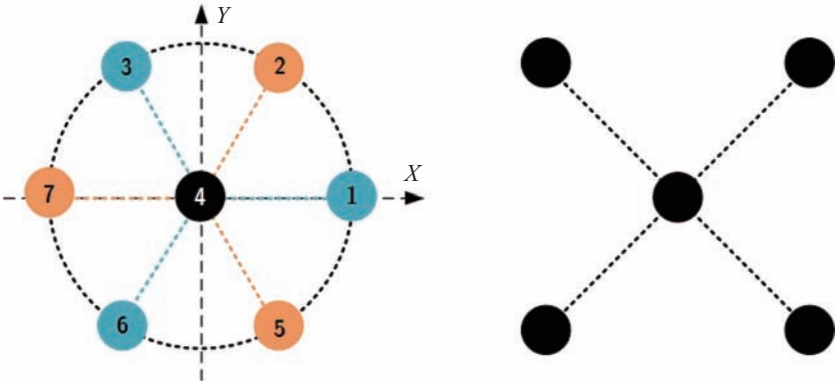

Fig. 2 Two examples of the centro-symmetrical array geometry.

We obtain the following equation if the seven-element array is indexed as in Fig. 2:

$$\boldsymbol{p}_i = -\boldsymbol{p}_{M-i+1},\ i = 1,2,\cdots,M \tag{2}$$

where M denotes the element count, which is odd. The array response vector of a sine wave signal is presented as follows:

$$\boldsymbol{v}(f,\theta,\phi) = [\mathrm{e}^{-\mathrm{j}\frac{2\pi}{\lambda}\boldsymbol{p}_1^{\mathrm{T}}\boldsymbol{a}}, \mathrm{e}^{-\mathrm{j}\frac{2\pi}{\lambda}\boldsymbol{p}_2^{\mathrm{T}}\boldsymbol{a}}, \cdots, \mathrm{e}^{-\mathrm{j}\frac{2\pi}{\lambda}\boldsymbol{p}_M^{\mathrm{T}}\boldsymbol{a}}]^{\mathrm{T}} = [\mathrm{e}^{-\mathrm{j}\frac{2\pi}{\lambda}\boldsymbol{p}_1^{\mathrm{T}}\boldsymbol{a}}, \mathrm{e}^{-\mathrm{j}\frac{2\pi}{\lambda}\boldsymbol{p}_2^{\mathrm{T}}\boldsymbol{a}}, \cdots, 1, \cdots, \mathrm{e}^{\mathrm{j}\frac{2\pi}{\lambda}\boldsymbol{p}_2^{\mathrm{T}}\boldsymbol{a}}, \mathrm{e}^{\mathrm{j}\frac{2\pi}{\lambda}\boldsymbol{p}_1^{\mathrm{T}}\boldsymbol{a}}]^{\mathrm{T}} \tag{3}$$

where f is the sine wave frequency, and λ is the wavelength correspondingly. The incident direction vector $\boldsymbol{a}$ was related to θ and ϕ.

We provide the signal model based on the abovementioned array. The received signal by the array at epoch t can be written as follows:

$$\boldsymbol{x}(t) = [x_1(t), x_2(t), \cdots, x_M(t)]^{\mathrm{T}} \tag{4}$$

where $x_i(t)$ denotes the received signal by the i-th element. In an interference environment, $\boldsymbol{x}(t)$ includes three components (i.e., desired satellite signal, interference, and noise). The desired signal and the interference can be regarded as far-field plane waves, while the noise is modeled to be white Gaussian and uncorrelated between different elements. The passing time of the signal over the array was generally far smaller than the reciprocal of the signal bandwidth, implying that the narrow band hypothesis was satisfied[5]. Thus, $\boldsymbol{x}(t)$ can be decomposed as follows:

$$\boldsymbol{x}(t) = s(t)\boldsymbol{v}_{\mathrm{s}} + \sum_{l=1}^{L} j_l(t)\boldsymbol{v}_{\mathrm{j,l}} + \boldsymbol{n}(t) \tag{5}$$

where $s(t)$ denotes the desired satellite signal; $\boldsymbol{v}_{\mathrm{s}}$ denotes its array response vector at the central frequency f_c; $j_l(t)$ is the l-th interference and $\boldsymbol{v}_{\mathrm{j,l}}$ the array response vector at f_c; and $\boldsymbol{n}(t)$ denotes the noise. Each component is presumed to be zero mean, which is reasonable in practice.

In SOP-PI, the received signal of each element was multiplied by a complex weight after being sampled, quantized, and digitally down-converted successively. The results of all the elements were then summed to form the output to be processed by the tracking loop[16]. The optimal weight vector was calculated on the minimum power criterion:

$$\boldsymbol{w}_{\mathrm{opt}} = \mathrm{argmin}_{\boldsymbol{w}}\{\boldsymbol{w}^{\mathrm{H}}\boldsymbol{R}\boldsymbol{w}\} \tag{6}$$

where $\boldsymbol{R}$ is the correlation matrix defined by

$$\boldsymbol{R} = \mathbb{E}\{\boldsymbol{x}(t)\boldsymbol{x}^{\mathrm{H}}(t)\} \tag{7}$$

The optimal weight vector was obtained as follows using the Lagrange multiplier technique:

$$\boldsymbol{w}_{\mathrm{opt}} = \Lambda\boldsymbol{R}^{-1}\boldsymbol{w}_{\mathrm{q}} \tag{8}$$

where

$$\boldsymbol{w}_{\mathrm{q}}{}^{\mathrm{H}} = \begin{bmatrix} 0 & \cdots & 0 & 1 & 0 & \cdots & 0 \end{bmatrix} \tag{9}$$

$$\Lambda = (\boldsymbol{w}_{\mathrm{q}}{}^{\mathrm{H}}\boldsymbol{R}^{-1}\boldsymbol{w}_{\mathrm{q}})^{-1} \tag{10}$$

Vector $\boldsymbol{w}_{\mathrm{q}}$ denotes the weight vector resulting in the quiescent beam pattern, with the value of 1 corresponding to the reference element[5].

3 Bias-Free Derivation of SOP-PI

In this section, we ignored the non-ideal factors of the antenna elements. Different from STAP, which attaches a Finite Impulse Response (FIR) filter to each element, and its nearly equivalence substitute SFAP in the frequency domain, SOP has a flat frequency response within the signal bandwidth; hence, the correlation function of the ranging codes is not distorted, resulting in no pseudorange biases. Therefore, in the rest of this paper, we focus on the

carrier phase biases, which is essential in most precision positioning applications such as RTK and Precise Point Positioning (PPP).

The mathematical derivation in this section shows that, for an array with a centro-symmetrical geometry, SOP-PI also naturally induces no biases to the carrier phase measurements.

Based on Eq. (5), $\boldsymbol{R}$ can be decomposed as follows:

$$\boldsymbol{R}=\boldsymbol{V}_j\boldsymbol{R}_j{\boldsymbol{V}_j}^{\mathrm{H}}+\sigma_n^2\boldsymbol{I} \tag{11}$$

where

$$\boldsymbol{V}_j=\left[\boldsymbol{v}_{j,1}\ \boldsymbol{v}_{j,2}\ \cdots\ \boldsymbol{v}_{j,L}\right] \tag{12}$$

$$[\boldsymbol{R}_j]_{pq}=\mathbb{E}\{j_p(t)j_q^*(t)\} \tag{13}$$

Scalar $[\boldsymbol{R}_j]_{pq}$ is the value in the p-th row and q-th column of $\boldsymbol{R}_j$. The desired satellite signal component is neglected because its power is well below the noise floor by at least 20 dB.

According to the matrix inversion lemma[17], we have

$$\boldsymbol{R}^{-1}=\frac{1}{\sigma_n^2}[\boldsymbol{I}-\boldsymbol{V}_j(\boldsymbol{I}+\frac{\boldsymbol{R}_j}{\sigma_n^2}{\boldsymbol{V}_j}^{\mathrm{H}}\boldsymbol{V}_j)^{-1}\frac{\boldsymbol{R}_j}{\sigma_n^2}{\boldsymbol{V}_j}^{\mathrm{H}}] \tag{14}$$

Substitute it to Eq. (8) we have

$$\boldsymbol{w}_{\mathrm{opt}}=\frac{\boldsymbol{\Lambda}}{\sigma_n^2}[\boldsymbol{I}-\boldsymbol{V}_j(\boldsymbol{I}+\frac{\boldsymbol{R}_j}{\sigma_n^2}{\boldsymbol{V}_j}^{\mathrm{H}}\boldsymbol{V}_j)^{-1}\frac{\boldsymbol{R}_j}{\sigma_n^2}{\boldsymbol{V}_j}^{\mathrm{H}}]\boldsymbol{w}_{\mathrm{q}} \tag{15}$$

Note that each column of $\boldsymbol{V}_j$ is a conjugate symmetric because of the array centro-symmetry:

$$\begin{aligned}{\boldsymbol{v}_{j,l}}^{\mathrm{H}}=[&\mathrm{e}^{\mathrm{j}\frac{2\pi}{\lambda_c}{\boldsymbol{p}_1}^{\mathrm{T}}\boldsymbol{a}_{j,l}},\ \cdots,\ \mathrm{e}^{\mathrm{j}\frac{2\pi}{\lambda_c}{\boldsymbol{p}_{(\boldsymbol{M}-1)/2}}^{\mathrm{T}}\boldsymbol{a}_{j,l}},\ 1,\\ &\mathrm{e}^{-\mathrm{j}\frac{2\pi}{\lambda_c}{\boldsymbol{p}_{(\boldsymbol{M}-1)/2}}^{\mathrm{T}}\boldsymbol{a}_{j,l}},\ \cdots,\ \mathrm{e}^{-\mathrm{j}\frac{2\pi}{\lambda_c}{\boldsymbol{p}_1}^{\mathrm{T}}\boldsymbol{a}_{j,l}}\ ]\end{aligned} \tag{16}$$

Accordingly, l varies from 1 to L. $\boldsymbol{v}_{j,p}^{\mathrm{H}}\boldsymbol{v}_{j,q}$ is real for any p and q ranging from 1 to L.

Consider two typical cases. In the first case, assume that the power of interference is far stronger than the noise. Note that in real scenarios, the interferences from different jammers or other kinds of sources can easily guarantee that $\boldsymbol{R}_j$ is non-singular. Thus, the $\boldsymbol{I}$ within the matrix inverse in Eq. (15) can be neglected, resulting in Eq. (15) to be simplified as follows:

$$\begin{aligned}\boldsymbol{w}_{\mathrm{opt}}=&\frac{\boldsymbol{\Lambda}}{\sigma_n^2}[\boldsymbol{I}-\boldsymbol{V}_j(\frac{\boldsymbol{R}_j}{\sigma_n^2}{\boldsymbol{V}_j}^{\mathrm{H}}\boldsymbol{V}_j)^{-1}\frac{\boldsymbol{R}_j}{\sigma_n^2}{\boldsymbol{V}_j}^{\mathrm{H}}]\boldsymbol{w}_{\mathrm{q}}=\\ &\frac{\boldsymbol{\Lambda}}{\sigma_n^2}[\boldsymbol{I}-\boldsymbol{V}_j({\boldsymbol{V}_j}^{\mathrm{H}}\boldsymbol{V}_j)^{-1}{\boldsymbol{V}_j}^{\mathrm{H}}]\boldsymbol{w}_{\mathrm{q}}\end{aligned} \tag{17}$$

The element of the p-th row and q-th column in matrix $\boldsymbol{V}_j^{\mathrm{H}}\boldsymbol{V}_j$ is $\boldsymbol{v}_{j,p}^{\mathrm{H}}\boldsymbol{v}_{j,q}$, resulting to both $\boldsymbol{V}_j^{\mathrm{H}}\boldsymbol{V}_j$ and $(\boldsymbol{V}_j^{\mathrm{H}}\boldsymbol{V}_j)^{-1}$ being real. This makes every column of the matrix $\boldsymbol{V}_j(\boldsymbol{V}_j^{\mathrm{H}}\boldsymbol{V}_j)^{-1}$ a conjugate symmetric vector. Note that all the elements of the $(M+1)/2$-th column of $\boldsymbol{V}_j^{\mathrm{H}}$ are 1; thus, the $(M+1)/2$-th column of $\boldsymbol{V}_j(\boldsymbol{V}_j^{\mathrm{H}}\boldsymbol{V}_j)^{-1}\boldsymbol{V}_j^{\mathrm{H}}$ is also a conjugate symmetric vector. Finally, considering that $\boldsymbol{\Lambda}$ is real, the optimal weight vector $\boldsymbol{w}_{\mathrm{opt}}$ also has a conjugate symmetrical form.

In the second case, no precondition exists about the interference strength, but it is presumed that each two of the L interferences are uncorrelated. Therefore, $\boldsymbol{R}_j$ is real and diagonal, such that the matrix $(\boldsymbol{I}+\frac{\boldsymbol{R}_j}{\sigma_n^2}\boldsymbol{V}_j^{\mathrm{H}}\boldsymbol{V}_j)^{-1}\frac{\boldsymbol{R}_j}{\sigma_n^2}$ is real. Through a reasoning process similar to that in the first case, $\boldsymbol{w}_{\mathrm{opt}}$ also has a conjugate symmetrical form. The abovementioned two cases cover most interference situations in practice, except those in which the interferences are not that strong and correlated with each other. Making this exception happen is very trivial; hence, it is ignored in this paper.

In the end of this section, we conclude that if $\boldsymbol{w}_{\mathrm{opt}}$ is a conjugate symmetrical vector, then no carrier phase biases will be induced. Let the desired satellite signal incident from (θ_s,ϕ_s), without considering the non-ideal factors of the array elements and the Radio Frequency (RF) channels. The transfer function of the array can then be written as follows:

$$H(\theta_s,\phi_s)=\boldsymbol{w}_{\mathrm{opt}}^{\mathrm{H}}\boldsymbol{v}_s(\theta_s,\phi_s) \tag{18}$$

Both $\boldsymbol{w}_{\mathrm{opt}}$ and $\boldsymbol{v}_s$ are conjugate symmetrical; thus, $H(\theta_s,\phi_s)$ is real in any incident direction. If $H(\theta_s,\phi_s)$ is positive, then the induced carrier phase bias is 0°. Otherwise, the bias is 180°.

A typical GNSS receiver uses an I/Q demodulator to extract the navigation data bits in the tracking loop, making the initial carrier phase of the received signal in the Phase Lock Loop (PLL) arbitrary and causing the 180° ambiguity in the carrier phase measurement[16, 18]. This ambiguity can be eliminated in the following frame synchronization process thorough checking the specific header word. In this sense, the 180° bias induced by the array is equivalent to 0° bias.

4 Influence of Array Perturbations on Carrier Phase Measurements

The abovementioned derivation concludes that, in the ideal case, by using a centro-symmetrical array geometry, SOP-PI will not induce carrier phase biases. However, in practice, various non-ideal factors are evitable. For instance, ideally, the amplitude (gain) and the phase (phase shift) of each antenna element should be identical. However, this is impossible in real manufactured antennas,

causing the array perturbations of element amplitude and phase. Moreover, ideally, the phase center of each element should coincide with the geometric center, but in practice, the phase center locates within a volume near the geometric center because of the element anisotropy, causing the array perturbation of the element phase center. To some extent, the non-ideal factors of the RF channels can be absorbed in the antenna elements before them. All these non-ideal factors can cause the bias-free conclusion above to no longer stand. A detailed analysis is provided below.

4.1 Perturbation model

The array perturbations of the element amplitude, phase, and phase center all affect the performance of SOP-PI by making the array response vector deviate from the ideal form given in Eq. (3). Therefore, they are considered together. Let the perturbation vector be

$$\boldsymbol{\rho}=\left[\boldsymbol{a}_{\Delta}^{\mathrm{T}}\ \boldsymbol{\varphi}_{\Delta}^{\mathrm{T}}\ \boldsymbol{p}_{x,\Delta}^{\mathrm{T}}\ \boldsymbol{p}_{y,\Delta}^{\mathrm{T}}\ \boldsymbol{p}_{z,\Delta}^{\mathrm{T}}\right]^{\mathrm{T}} \tag{19}$$

where

$$[\boldsymbol{a}_{\Delta}]_m=\Delta a_m,\qquad m=1,2,\cdots,M \tag{20}$$

$$[\boldsymbol{\varphi}_{\Delta}]_m=\Delta\varphi_m,\qquad m=1,2,\cdots,M \tag{21}$$

$$[\boldsymbol{p}_{x,\Delta}]_m=\Delta p_{x,m},\qquad m=1,2,\cdots,M \tag{22}$$

$$[\boldsymbol{p}_{y,\Delta}]_m=\Delta p_{y,m},\qquad m=1,2,\cdots,M \tag{23}$$

$$[\boldsymbol{p}_{z,\Delta}]_m=\Delta p_{z,m},\qquad m=1,2,\cdots,M \tag{24}$$

Therein, Δa_m and $\Delta\varphi_m$ denote the amplitude and the phase perturbations of the m-th element, respectively. They are different for different elements most of the time, leading to the element inconsistency. Parameters $\Delta p_{x,m}$, $\Delta p_{y,m}$, and $\Delta p_{z,m}$ denote the phase center perturbations of the m-th element along the three axes of the antenna coordinate system. The statistical probability model given in Ref. [5] was adopted herein, in which $\boldsymbol{\rho}$ was modeled as a Gaussian vector whose probability density function is given by

$$p_{\boldsymbol{\rho}}=\frac{1}{(2\pi)^{\frac{5M}{2}}|\boldsymbol{\Lambda}_{\boldsymbol{\rho}}|^{\frac{1}{2}}}\exp\{-\frac{1}{2}(\boldsymbol{\rho}-\boldsymbol{\rho}_{\mathbf{0}})^{\mathrm{T}}\boldsymbol{\Lambda}_{\boldsymbol{\rho}}(\boldsymbol{\rho}-\boldsymbol{\rho}_{\mathbf{0}})\} \tag{25}$$

where $\boldsymbol{\rho}_{\mathbf{0}}$ and $\boldsymbol{\Lambda}_{\rho}$ are the mean and correlation matrix of $\boldsymbol{\rho}$, respectively. For convenience, we write the phase center perturbation vector of the m-th element as follows:

$$\boldsymbol{p}_{\Delta,m}=\left[\Delta p_{x,m}\ \Delta p_{y,m}\ \Delta p_{z,m}\right]^{\mathrm{T}} \tag{26}$$

Then, with the effect of the array perturbations, the array response vector given in Eq. (3) is modified to

$$\boldsymbol{v}(\theta,\phi,\boldsymbol{\rho})=\begin{bmatrix}(1+\Delta a_1)\mathrm{e}^{\mathrm{j}\Delta\varphi_1}\mathrm{e}^{-\mathrm{j}\frac{2\pi}{\lambda_c}(\boldsymbol{p}_1+\boldsymbol{p}_{\Delta,1})^{\mathrm{T}}\boldsymbol{a}}\\(1+\Delta a_2)\mathrm{e}^{\mathrm{j}\Delta\varphi_2}\mathrm{e}^{-\mathrm{j}\frac{2\pi}{\lambda_c}(\boldsymbol{p}_2+\boldsymbol{p}_{\Delta,2})^{\mathrm{T}}\boldsymbol{a}}\\\cdots\\(1+\Delta a_M)\mathrm{e}^{\mathrm{j}\Delta\varphi_M}\mathrm{e}^{-\mathrm{j}\frac{2\pi}{\lambda_c}(\boldsymbol{p}_M+\boldsymbol{p}_{\Delta,M})^{\mathrm{T}}\boldsymbol{a}}\end{bmatrix} \tag{27}$$

Thus, all the columns of $\boldsymbol{V}_j$ are no longer conjugate-symmetrical, and so is $\boldsymbol{w}_{\mathrm{opt}}$, thereby making the bias-free condition not any more satisfied.

4.2 Simulation analysis

We investigated herein how exactly the array perturbations affect the carrier phase biases. Analytical closed forms were difficult to obtain; hence, the Monte Carlo simulation method was used. Assume that the elements of $\boldsymbol{\rho}$ all have zero means and are independent of each other (i.e., $\boldsymbol{\rho}_{\mathbf{0}}$ is a zero vector, and $\boldsymbol{\Lambda}_{\boldsymbol{\rho}}$ is diagonal). Further assume that the standard deviations of Δa_m and $\Delta\varphi_m$ (i.e., σ_{amp} and σ_{phase}) are the same for all the elements, while the standard deviations of $\Delta p_{x,m}$, $\Delta p_{y,m}$, and $\Delta p_{z,m}$ are all σ_{xyz} for all the elements. The B1 signal of the Beidou Satellite Navigation System which has a central frequency of 1561.098 MHz[19], is taken as an example of the desired satellite signal. Three jammers radiating a White Gaussian Noise (WGN) interference covering the whole sampling bandwidth of 30 MHz with an Interference-to-Noise-Ratio (INR) of 60 dB were positioned in the scenario, as presented in Table 1.

First, the situation with no array perturbations was investigated as a reference. Using the optimal weight obtained from Eq. (15), the beam pattern of the array antenna can be calculated using Eq. (18), with the gain and phase shift given by the following two equations, respectively:

$$G(\theta_s,\phi_s)=20\log|\boldsymbol{w}_{\mathbf{opt}}^{\mathrm{H}}\boldsymbol{v}_s| \tag{28}$$

$$\varphi_e(\theta_s,\phi_s)=\arctan\frac{\Im(\boldsymbol{w}_{\mathbf{opt}}^{\mathrm{H}}\boldsymbol{v}_s)}{\Re(\boldsymbol{w}_{\mathbf{opt}}^{\mathrm{H}}\boldsymbol{v}_s)} \tag{29}$$

where $\Re(\cdot)$ and $\Im(\cdot)$ denote the operations of extracting the real and imaginary parts, respectively. The effect of the 180° ambiguity mentioned earlier was avoided using

Table 1 Interference scenario used in this paper. All the three jammers radiate a white Gaussian noise interference.

	θ (°)	ϕ (°)	INR (dB)
jammer 1	30	50	60
jammer 2	50	170	60
jammer 3	75	300	60

the calculation method of Eq. (29). Figure 3 presents the gains and phase shifts of the beam pattern, where the red blocks represent the locations of the jammers. While nulls are formed toward these jammers, no carrier phase bias is induced in all the directions in the upper hemisphere.

Next, an instance of $\boldsymbol{\rho}$ is randomly generated according to the abovementioned perturbation model. Figure 4 presents the resulted beam pattern, which shows that the gains of the pattern are distorted compared with the ideal one above, and the carrier phase biases emerge.

Figure 4 also illustrates that the smaller the gain in a certain direction, the larger the phase bias in the same direction tends to be. The desired satellite signal in these directions with very low gains will be attenuated by a great deal, causing the receivers' incapability of tracking or, even, loss of track. We define G_t as the gain threshold based on this consideration. The directions in which $G(\theta,\phi)$ is bigger than G_t are called effective directions, while those otherwise are called ineffective directions. It is assumed that only in the effective directions can the desired satellite signals be steadily tracked; hence, only the carrier phase biases in these directions were worth considering. The mean and the standard deviation of the carrier phase biases in the effective directions of one certain beam pattern are specifically defined as follows:

$$\varphi_{e,\mathrm{mean}} = \frac{\iint_{S_{\mathrm{eff}}} \varphi_e(\theta,\phi)\sin\theta \mathrm{d}\theta\mathrm{d}\phi}{\iint_{S_{\mathrm{eff}}} \sin\theta \mathrm{d}\theta\mathrm{d}\phi} \tag{30}$$

$$\varphi_{e,\mathrm{std}} = \sqrt{\frac{\iint_{S_{\mathrm{eff}}} [\varphi_e(\theta,\phi)-\varphi_{e,\mathrm{mean}}]^2\sin\theta \mathrm{d}\theta\mathrm{d}\phi}{\iint_{S_{\mathrm{eff}}} \sin\theta \mathrm{d}\theta\mathrm{d}\phi}} \tag{31}$$

where S_{eff} denotes the area made up of all the effective directions in the upper hemisphere shown in Fig. 4. $\varphi_{e,\mathrm{mean}}$ represents the total offset of the carrier phase biases in S_{eff}, while $\varphi_{e,\mathrm{std}}$ represents the possible carrier phase bias differences in different directions, both of which influence the positioning performance. Thus, we used both of them to measure the severity of the biases in the following.

4.2.1 Element phase center perturbation

The array perturbations of the element phase center,

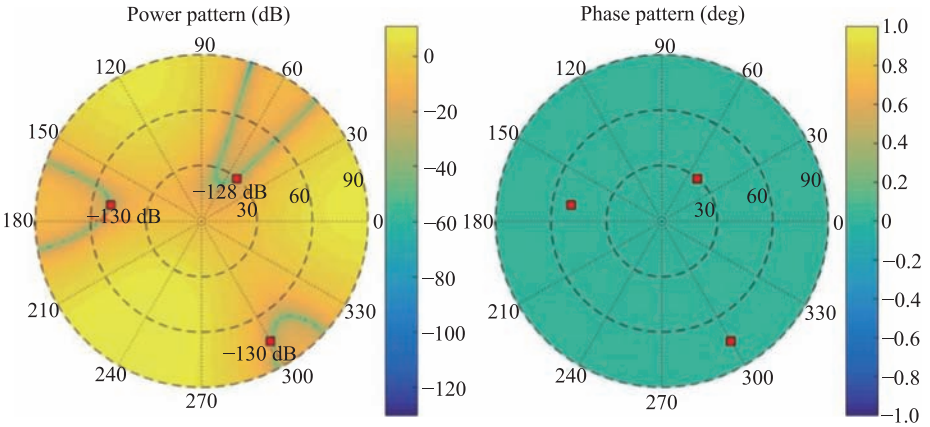

Fig. 3 Gains and phase shifts of the beam pattern in the ideal case with no array perturbations.

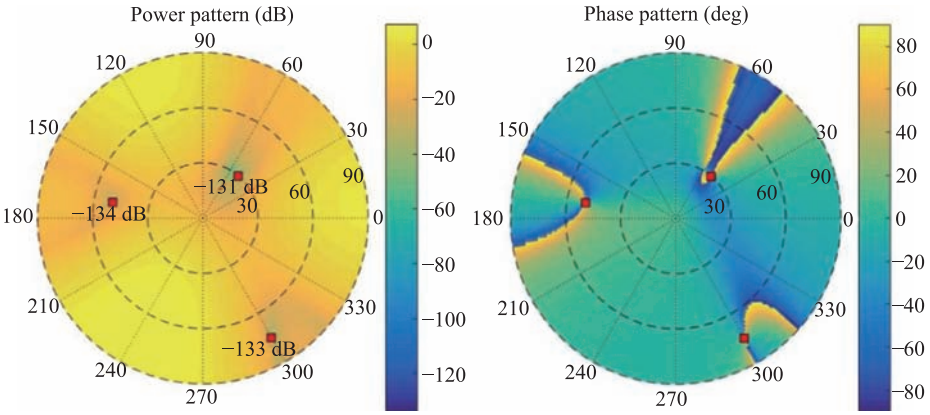

Fig. 4 Gains and phase shifts of the beam pattern with one randomly generated instance of array perturbations.

amplitude, and phase were individually investigated. First, assume that σ_{amp} and σ_{phase} were both zero, while σ_{xyz} varied. A total of 500 random trials were performed under each value of σ_{xyz}. In each trial, $\boldsymbol{p}_{\Delta,m}$ for m ranging from 1 to M was randomly generated according to the Gaussian probability model given before, then $\varphi_{e,\text{mean}}$ and $\varphi_{e,\text{std}}$ were calculated. Figure 5 presents how the 500-trial average $\varphi_{e,\text{std}}$ varied with σ_{xyz} under different G_t. The graphic results of $\varphi_{e,\text{mean}}$ were omitted because its 500-trial averages were all near zero. Figure 5 depicts that $\varphi_{e,\text{std}}$ increased when σ_{xyz} increased. In other words, the carrier phase biases became more severe. Meanwhile, if the array perturbations of the element phase center were strictly restricted, then the carrier phase biases can be reduced to an acceptable level. Figure 5 also implies that raising G_t helped reduce the carrier phase biases (i.e., abandoning the satellite signals with low SNRs helped avoid the incident directions with large carrier phase biases). The price paid was that the number of available visible satellites may decrease. As a step further, we investigated the relation of the carrier phase biases with the interference scenario. Figure 6 presents the $\varphi_{e,\text{std}}$ variations over σ_{xyz} while the jammers in Table 1 were successively added one by one with G_t fixed to -10 dB. In conclusion, more jammers made the carrier phase biases more severe.

4.2.2 Element amplitude perturbation

Similarly, the array perturbation of the element amplitude was investigated on its own. Let us set σ_{phase} and σ_{xyz} to zero, and simulate the variations of $\varphi_{e,\text{mean}}$ and $\varphi_{e,\text{std}}$ over σ_{amp} under different values of G_t and numbers of jammers. Figures 7 and 8 show the results. The 500-trial averages of $\varphi_{e,\text{mean}}$ under different σ_{amp} were all near zero; therefore, the graphic results of $\varphi_{e,\text{mean}}$ were omitted. $\varphi_{e,\text{std}}$ increased with σ_{amp}, as well as the numbers of jammers.

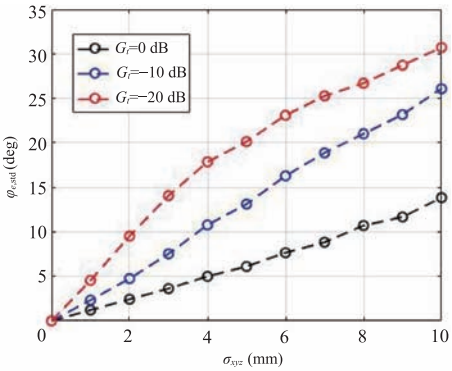

Fig. 5 500-trial average results of $\varphi_{e,\text{std}}$ variations over σ_{xyz} with different values of G_t.

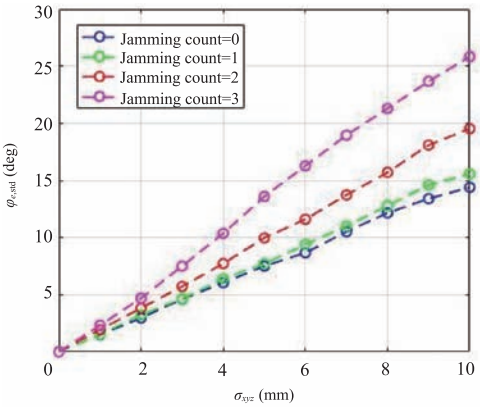

Fig. 6 500-trial average results of $\varphi_{e,\text{std}}$ variations over σ_{xyz} with different numbers of jammers with G_t fixed to -10 dB.

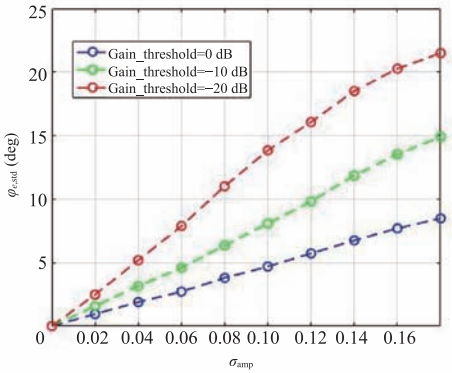

Fig. 7 500-trial average results of the $\varphi_{e,\text{std}}$ variations over σ_{amp} with different values of G_t.

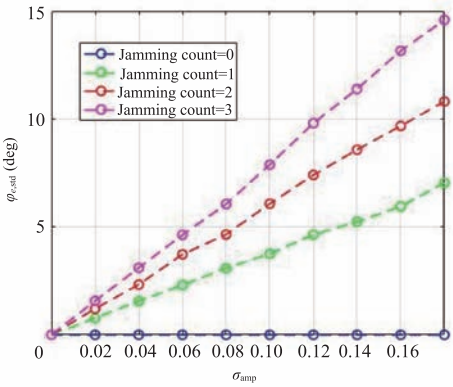

Fig. 8 500-trial average results of the $\varphi_{e,\text{std}}$ variations over σ_{amp} with different numbers of jammers.

4.2.3 Element phase perturbation

The impact of the array perturbation of the element phase on the carrier phase biases was different from that of

the array perturbation of the element phase center or amplitude. Figures 9 and 10 present the 500-trial average variations of $\varphi_{e,\mathrm{mean}}$ and $\varphi_{e,\mathrm{std}}$ over σ_{phase} with different numbers of jammers. The increase of σ_{phase} did not aggravate the carrier phase bias severity. Figure 11 depicts the gains and the phase shifts of the beam pattern under a random group of element phase perturbations. The array introduced the same carrier phase bias in all the incident directions, which happened to be the phase perturbation of the reference element.

This phenomenon can be theoretically explained in mathematics. If the array phase perturbation matrix is defined as follows:

$$\boldsymbol{P}=\mathrm{diag}\{\mathrm{e}^{\mathrm{j}\Delta\varphi_1},\mathrm{e}^{\mathrm{j}\Delta\varphi_2},\cdots,\mathrm{e}^{\mathrm{j}\Delta\varphi_M}\} \tag{32}$$

then, the array response matrix of the interference components after perturbation is

$$\tilde{\boldsymbol{V}}_j=\boldsymbol{P}\boldsymbol{V}_j \tag{33}$$

By plugging Eq. (33) into Eq. (15), the optimal weight vector turns to

$$\tilde{\boldsymbol{w}}_{\mathrm{opt}}=\frac{\boldsymbol{\Lambda}}{\sigma_n^2}[\boldsymbol{I}-\tilde{\boldsymbol{V}}_j(\boldsymbol{I}+\frac{\boldsymbol{R}_j}{\sigma_n^2}\tilde{\boldsymbol{V}}_j^{\mathrm{H}}\tilde{\boldsymbol{V}}_j)^{-1}\frac{\boldsymbol{R}_j}{\sigma_n^2}\tilde{\boldsymbol{V}}_j^{\mathrm{H}}]\boldsymbol{w}_{\mathrm{q}}=\mathrm{e}^{-\mathrm{j}\Delta\varphi_{(M+1)/2}}\boldsymbol{P}\boldsymbol{w}_{\mathrm{opt}} \tag{34}$$

The transfer function after perturbation can then be presented as follows:

$$\tilde{H}(\theta_s,\phi_s)=\tilde{\boldsymbol{w}}_{\mathrm{opt}}^{\mathrm{H}}\boldsymbol{P}\boldsymbol{v}_s(\theta_s,\phi_s)=\mathrm{e}^{\mathrm{j}\Delta\varphi_{(M+1)/2}}H(\theta_s,\phi_s) \tag{35}$$

Once $\Delta\varphi_{(M+1)/2}$ is measured, the corresponding carrier phase bias can be eliminated through compensation at the tracking output of the receiver.

4.3 Summary and discussion

The simulation results obtained in this section are summarized as follows:

- The array perturbations of the element phase center and the amplitude introduced carrier phase biases to the receiver by disturbing the conjugate symmetry of the array response vector.

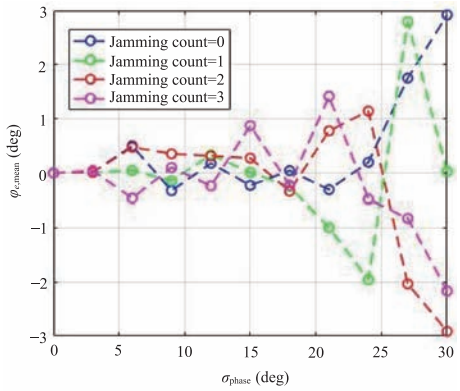

Fig. 9 500-trial average results of the $\varphi_{e,\mathrm{mean}}$ variations over σ_{phase} with different numbers of jammers and G_t fixed to -10 dB.

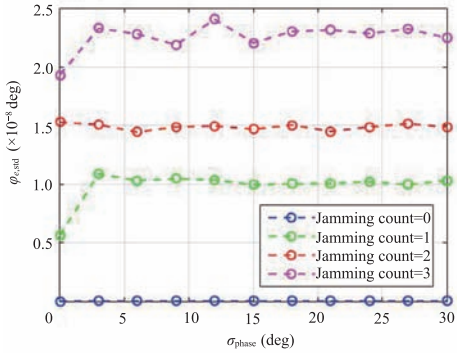

Fig. 10 500-trial average results of the $\varphi_{e,\mathrm{std}}$ variations over σ_{phase} with different numbers of jammers and G_t fixed to -10 dB.

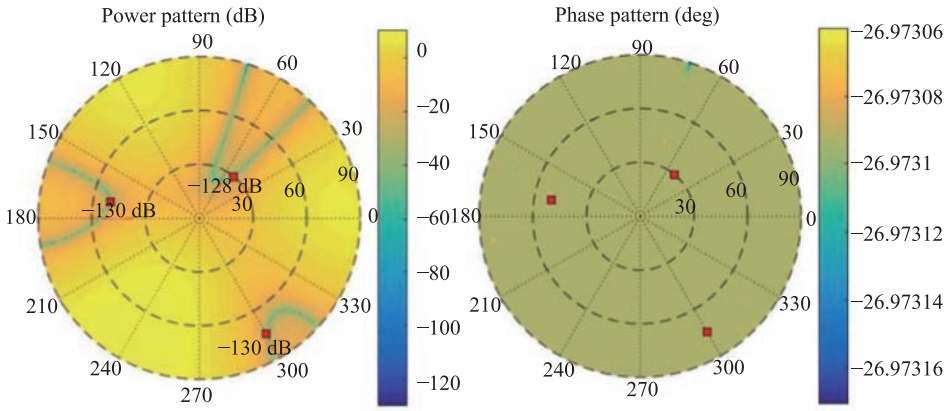

Fig. 11 Gain and phase shift of the beam pattern under one randomly generated instance of array phase perturbations while the phase perturbation of the reference element is $-26.97°$.

- Reducing the array perturbation degree of the element phase center and the amplitude, which meant making the element phase centers and amplitudes as much as symmetric, helped reduce the severity of the carrier phase biases.
- Abandoning the received satellite signals with low SNRs helped avoid the directions with large carrier phase biases in the upper hemisphere.
- The more complicated the interference scenario, the more severe the carrier phase biases.
- The array perturbation of the element phase only introduced the same carrier phase bias in all the directions in the upper hemisphere, which happened to be the phase perturbation of the reference element, thus can be compensated.

Equation (27) shows that the array perturbations of both the element phase center and the element phase introduced extra phase shifts to the array response vector. However, they led to different results to the final carrier phase biases because the phase shifts resulting from the element phase center perturbation were direction-dependent, while those resulting from the element phase perturbation were not. This result implied that the anisotropy of the element phase will make the carrier phase biases more severe.

Aside from the anisotropy of the element phase, the anisotropy of the element amplitude and the phase center and the frequency dispersion effect of the antenna elements were also ignored in this study. That these non-ideal factors will further deteriorate the carrier phase biases is reasonable; hence, they should be constrained as much as possible.

In conclusion, strict constraints on the element phase center and the amplitude perturbations should be made to meet the high-precision demand. In practice, they can hopefully be met by careful design and manufacture of each antenna element, as well as decreasing the mutual coupling effect by adopting small antenna elements and increasing the inter-element spacing.

5 Finite-Sample Effect

Ideally, the optimal weight vector $\boldsymbol{w}_{\rm opt}$ is calculated from the ideal correlation matrix $\boldsymbol{R}$. However, the correlation matrix in the practical operation of the algorithm is estimated from finite sample snapshots by averaging:

$$\hat{\boldsymbol{R}}=\frac{1}{K}\sum_{k=0}^{K-1}\boldsymbol{x}[n+k]\boldsymbol{x}^{\rm H}[n+k] \tag{36}$$

where $\boldsymbol{x}[n]$ is the snapshot of $\boldsymbol{x}(t)$ at the n-th sampling period, while K is the number of snapshots used to estimate $\hat{\boldsymbol{R}}$. Perturbations will exist between $\hat{\boldsymbol{R}}$ and $\boldsymbol{R}$ because of the limited samples (i.e., the finite-sample effect), making $\hat{\boldsymbol{w}}_{\rm opt}$ no longer a conjugate symmetrical, and resulting in the carrier phase measurements to be biased. Figure 12 presents the 500-trial average results of the $\varphi_{e,\rm std}$ variations over K in the interference scenario given by Table 1, both with and without the array perturbations, respectively. The array perturbations of the element amplitude, phase, and phase center were randomly generated from the Gaussian model and different for each trial. The 500-trial average of $\varphi_{e,\rm mean}$ was near to zero under each K; hence, the graphic results were omitted. Even without array perturbations, the carrier phase biases were induced because of the finite-sample effect. Although increasing K can reduce the carrier phase biases, this costs the price of less rapid weight updating period and more computational complexities.

Two countermeasures can be adopted toward the issue of finite-sample effect: diagonal loading and forward-backward averaging.

5.1 Diagonal loading

Diagonal loading is a common practice in many adaptive array applications. It means adding a constant power on the diagonal of the correlation matrix, just as below:

$$\boldsymbol{R}_{dl}=\hat{\boldsymbol{R}}+\sigma_{dl}^2\boldsymbol{I} \tag{37}$$

where σ_{dl}^2 denotes the power of diagonal loading, and is usually determined by its ratio with respect to σ_n^2:

$$\sigma_{dl}^2=\mathrm{DLNR}\cdot\sigma_n^2 \tag{38}$$

Diagonal loading is equivalent to artificially raising the uncorrelated noise power of all the antenna elements. It

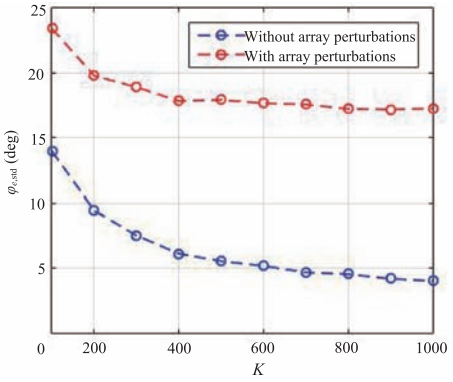

Fig. 12 500-trial average results of the $\varphi_{e,\rm std}$ variations over K with or without array perturbations, $G_t=-10$ dB, $\sigma_{xyz}=5$ mm, $\sigma_{\rm amp}=0.05$, and $\sigma_{\rm phase}=30°$.

can make the algorithm more robust to the perturbations of the correlation matrix, as well as prevent the correlation matrix from being ill-conditioned or even singular[20, 21]. The principle can be explained by an eigenvalue analysis[5].

Similarly, we used Monte Carlo simulations to investigate how diagonal loading improves the carrier phase biases induced by the finite-sample effect in SOP-PI. The simulation conditions remained the same with the above, except that K is fixed to 300. Figure 13 presents the 500-trial average results of the $\varphi_{e,\mathrm{std}}$ variations over the DLNR. The 500-trial average $\varphi_{e,\mathrm{mean}}$ was again near to zero under each DLNR; hence, the graphic results were not shown. Compared with Fig. 12, the carrier phase biases became less severe when the DLNR increased, but the biases induced by the array perturbations were still not reduced. In practice, the DLNR should be forbidden from being very large, because a large DLNR may reduce the null depths of the beam pattern. A level approximately 20 dB is typically suggested.

5.2 Forward-backward averaging

The array response vector is a conjugate symmetrical because of the centro-symmetry of the array geometry, and so is the ideal snapshot of the received signal when the noise is neglected:

$$\boldsymbol{x}_{\mathrm{id}}[n]=\boldsymbol{J}\boldsymbol{x}_{\mathrm{id}}{}^{*}[n] \tag{39}$$

where $\boldsymbol{J}$ is the exchange matrix, and multiplying it on the left of a column vector obtains the reversed order vector.

The backward snapshot is defined as follows if Eq. (36) is called forward averaging:

$$\boldsymbol{x}_{J}[n]=\boldsymbol{J}\boldsymbol{x}^{*}[n] \tag{40}$$

Backward averaging is then presented as

$$\hat{\boldsymbol{R}}_{b}=\sum_{k=0}^{K-1}\boldsymbol{x}_{J}[n+k]\boldsymbol{x}_{J}{}^{\mathrm{H}}[n+k] \tag{41}$$

Finally, the estimated correlation matrix obtained through the forward-backward averaging is

$$\hat{\boldsymbol{R}}_{fb}=\frac{1}{2}(\hat{\boldsymbol{R}}+\hat{\boldsymbol{R}}_{b})=\frac{1}{2}(\hat{\boldsymbol{R}}+\boldsymbol{J}\hat{\boldsymbol{R}}^{*}\boldsymbol{J}) \tag{42}$$

This is then used to calculate the weight vector according to Eq. (8)[5, 22].

Monte Carlo simulations were performed under the same conditions as above, except for the DLNR being fixed to 10 dB, and the forward-backward averaging adopted. Figure 14 shows the 500-trial average results of the $\varphi_{e,\mathrm{std}}$ variations over K. Again, the 500-trial average $\varphi_{e,\mathrm{mean}}$ is near to zero; thus, the graphic results are omitted. When the array perturbations are absent, the carrier phase biases are also absent under all values of K. However, after the array perturbations are added, the carrier phase biases are not reduced compared with Fig. 12 or became even worse, which may be because the array perturbations were spread between the two centro-symmetrical elements.

Diagonal loading must be adopted in practice instead because of the extra computational complexity and the array perturbation spreading introduced by the forward-backward averaging.

6 Conclusion

This study deepens the understanding of SOP-PI by pointing out that, if an array geometry with centro-symmetry is adopted, whether the receiver measurements, especially the carrier phase measurements, will satisfy certain high-precision applications mainly depends on the degree of the array perturbations of the element amplitude

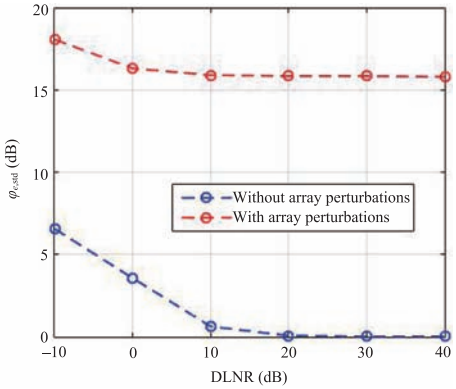

Fig. 13 500-trial average results of the $\varphi_{e,\mathrm{std}}$ variations over DLNR with $K=300$, $G_t=-10$ dB, $\sigma_{xyz}=5$ mm, $\sigma_{\mathrm{amp}}=0.05$, and $\sigma_{\mathrm{phase}}=30^{\circ}$.

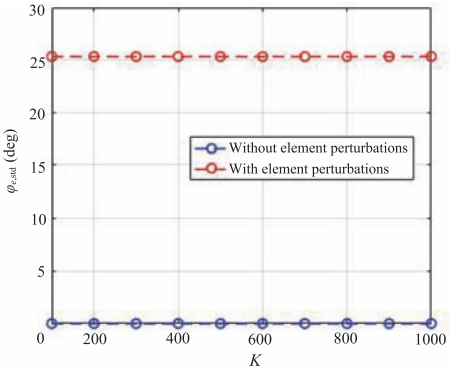

Fig. 14 500-trial average results of the $\varphi_{e,\mathrm{std}}$ variations over K using forward-backward averaging with or without array perturbations, while DLNR=10 dB, $G_t=-10$ dB, $\sigma_{xyz}=5$ mm, $\sigma_{\mathrm{amp}}=0.05$, and $\sigma_{\mathrm{phase}}=30^{\circ}$.

and the phase center. The algorithm itself is not the source of the measurement biases as long as diagonal loading or forward-backward averaging is used to counter the finite-sample effect. SOP-PI can be adopted if the antenna manufacturing technique or the compensation methods are good enough to lower these degrees to meet the application demands; otherwise, more complex algorithms, such as minimum variance distortionless response and STAP, should be used instead.

Acknowledgment

This work was supported by the National Natural Science Foundation of China (No. U1333203) and the Civil Aviation Administration of China (No. MHRD20140102).

References

[1] R. Sklar, Interference mitigation approaches for the global positioning system, *Lincoln Laboratory Journal,* vol. 14, no. 2, pp. 167–179, 2003.

[2] M. Cuntz, A. Konovaltsev, and M. Meurer, Concepts, development, and validation of multiantenna GNSS receivers for resilient navigation, *Proceedings of the IEEE,* vol. 104, no. 6, pp. 1288–1301, 2016.

[3] J. Gupta, M. Weiss, and W. Morrison, Desired features of adaptive antenna arrays for GNSS receivers, *Proceedings of the IEEE*, vol. 104, no. 6, pp. 1195–1206, 2016.

[4] C. Fernández-Prades, J. Arribas, and P. Closas, Robust GNSS receivers by array signal processing: Theory and implementation, *Proceedings of the IEEE*, vol. 104, no. 6, pp. 1207–1220, 2016.

[5] V. Trees and L. Harry, *Optimum Array Processing: Part IV of Detection, Estimation and Modulation Theory*. Wiley, 2002.

[6] M. Zoltowski and A. Gecan, Advanced adaptive null steering concepts for GPS, in *IEEE Military Communications Conference Record*, 1995, pp. 1214–1218.

[7] R. Fante and J. Vaccaro, Wideband cancellation of interference in a GPS receive array, *IEEE Transactions on Aerospace and Electronic Systems*, vol. 36, no. 2, pp. 549–564, 2000.

[8] I. Gupta and T. Moore, Space-frequency adaptive processing (SFAP) for radio frequency interference mitigation in spread-spectrum receivers, *IEEE Transactions on Antennas and Propagation*, vol. 52, no. 6, pp. 1611–1615, 2004.

[9] J. Rife, S. Khanafseh, S. Pullen, D. Lorenzo, U. Kim, M. Koenig, T. Chiou, B. Kempny, and B. Pervan, Navigation, interference suppression, and fault monitoring in the sea-based joint precision approach and landing system, *Proceedings of the IEEE*, vol. 96, no. 12, pp. 1958–1975, 2008.

[10] A. OBrien and I. Gupta, Mitigation of adaptive antenna induced bias errors in GNSS receivers, *IEEE Transactions on Aerospace and Electronic Systems*, vol. 47, no. 1, pp. 524–538, 2009.

[11] S. Daneshmand, Precise calibration of a GNSS antenna array for adaptive beamforming applications, *Sensors*, vol. 14, pp. 9669–9691, 2014.

[12] A. O'Brien, Adaptive antenna arrays for precision GNSS receivers, Ph D dissertation, Dept. Electrical and Computer Engineering, The Ohio State University, USA, 2009.

[13] I. Gupta, C. Church, A. O'Brien, and C. Slick, Prediction of antenna and antenna electronics induced biases in GNSS receivers, in *Proc. 2007 National Technical Meeting of The Institute of Navigation*, Monterey, CA, USA, 2007, pp. 650-656.

[14] C. Church, Estimation of adaptive antenna induced phase biases in global navigation satellite systems receiver measurements, PhD dissertation, Dept. Electrical and Computer Engineering, The Ohio State University, USA, 2009.

[15] C. Chuang and I. Gupta, On-the-fly estimation of antenna induced biases in SFAP based GNSS antenna arrays, *Navigation*, vol. 61, no. 4, pp. 323–330, 2014.

[16] E. Kaplan and C. Hegarty, *Understanding GPS : Principles and Applications*. Artech House, 2005.

[17] K. Petersen and M. Pedersen, *The Matrix Cookbook*. Technical University of Denmark, 2008.

[18] P. Misra and P. Enge, *Global Positioning System: Signals, Measurements, and Performance*. Ganga-Jamuna, 2011.

[19] China Satellite Navigation Office, BeiDou navigation satellite system signal in space interface control document, open service signal (version 2.1), Available: http://www.beidou.gov.cn/attach/2016/11/07/21212.pdf.

[20] B. Carlson, Covariance matrix estimation errors and diagonal loading in adaptive arrays, *IEEE Transactions on Aerospace and Electronic Systems*, vol. 24, no.4, pp. 397–401, 1988.

[21] J. Li, P. Stoica, and Z. Wang, On robust Capon beamforming and diagonal loading, *IEEE Transactions on Signal Processing*, vol. 51, no. 7, pp.1702–1715, 2003.

[22] G. Carrie, F. Vincent, T. Deloues, and D. Pietin, Stabilizing the phase response of blind array processors for GNSS interference cancellation, *Matrix*, vol. 3, no. 3, pp. 319–323, 2006.

Hailong Xu is a PhD candidate in the Department of Electronic Engineering, Tsinghua University, China. His current research focuses on GNSS high-precision positioning, adaptive array processing for anti-jamming, and simulation techniques by GPU computing. He received the BS degree from Tsinghua University in 2011.

Xiaowei Cui is an associate professor at the Department of Electronic Engineering, Tsinghua University, China. He is a member of the Expert Group of China BeiDou Navigation Satellite System. His research interests include robust GNSS signal processing, multipath mitigation techniques, and high-precision positioning. He obtained both the BS and PhD degrees in electronic engineering from Tsinghua University in 1999 and 2004, respectively.

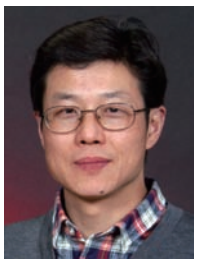

Mingquan Lu is a professor of the Department of Electronic Engineering, Tsinghua University, China. He is the director of Tsinghua Position, Navigation and Timing Center, and a member of the Expert Group of China BeiDou Navigation Satellite System. His current research interests include GNSS signal design and analysis, GNSS signal processing and receiver development, and GNSS system modeling and simulation. He received the MS degree in electronic engineering from the University of Electronic Science and Technology of China in 1993.